

Article

Comparison of the Grain-Refining Efficiencies of Ti and LaB₆ Inoculants in Additively Manufactured 2024 Aluminum Alloy: The Important Role of Solutes

Qiyang Tan , Yu Yin  and Ming-Xing Zhang *

School of Mechanical and Mining Engineering, The University of Queensland, St. Lucia, QLD 4072, Australia; q.tan@uq.edu.au (Q.T.); yu.yin@uq.edu.au (Y.Y.)

* Correspondence: mingxing.zhang@uq.edu.au; Tel.: +61-7-3346-8709

Abstract: The present work aims to boost our understanding of factors governing the grain-refining efficiency of inoculation treatments by comparing the grain-refining efficiencies of two inoculators: Ti nanoparticles and LaB₆ nanoparticles, in a 2024 Al alloy during additive manufacturing (AM). Experimental results obtained by scanning electron microscopy show that the LaB₆ nanoparticle possessed almost no refining effect on the alloy, with the addition content ranging from 0.5 wt.% to 2 wt.%. Conversely, the Ti nanoparticle resulted in a more pronounced refinement and a fine, fully equiaxed microstructure at 1 wt.% Ti addition. Based on transmission electron microscopy analysis, the higher refining efficiency of Ti inoculation was ascribed to the incorporation of both Ti solute and the in situ-formed L₁₂-Al₃Ti nucleation particles. The former significantly increased the overall undercooling ahead of the growing Al grain, which ensured the activation of heterogeneous nucleation on the L₁₂-Al₃Ti nanoparticles, leading to grain refinement. This work highlights that despite the addition of nucleation particles, the incorporation of appropriate solutes to generate sufficient undercooling is the prerequisite for the activation of heterogeneous nucleation in AM.

Keywords: additive manufacturing; aluminum alloys; grain refinement; EBSD; TEM



Citation: Tan, Q.; Yin, Y.; Zhang, M.-X. Comparison of the Grain-Refining Efficiencies of Ti and LaB₆ Inoculants in Additively Manufactured 2024 Aluminum Alloy: The Important Role of Solutes. *Metals* **2023**, *13*, 1490. <https://doi.org/10.3390/met13081490>

Academic Editor: Babak Shalchi Amirkhiz

Received: 26 July 2023

Revised: 14 August 2023

Accepted: 17 August 2023

Published: 19 August 2023



Copyright: © 2023 by the authors. Licensee MDPI, Basel, Switzerland. This article is an open access article distributed under the terms and conditions of the Creative Commons Attribution (CC BY) license (<https://creativecommons.org/licenses/by/4.0/>).

1. Introduction

Additive manufacturing (AM), such as selective laser melting (SLM) and direct energy deposition (DED), has emerged as a transformative technology in the production of advanced engineering metallic materials by offering rapid fabrication with high design freedom for part complexity [1]. However, the bottleneck problem of this frontier technique is the high tendency to form large, textured, columnar structures within the components fabricated by AM. This is attributed to the extremely large thermal gradient and the high cooling rate during AM solidification, which favor epitaxial grain growth [2,3]. In addition, partial remelting of the previous layer is involved during the successive layer-wise fabrication. The grains in the new layer tend to nucleate and grow epitaxially from the previous layer due to the low nucleation barrier, forming extensive columnar grains that span over multiple layers [4–6]. Such columnar structures not only cause significant anisotropy in the mechanical properties but also increased hot-cracking susceptibility under the high thermal shock during AM [7,8]. In comparison, a homogeneous and equiaxed microstructure is known not only to provide isotropic and improved mechanical properties but also to more readily accommodate strain, reducing hot-cracking [9,10]. Thus, converting columnar grains into fine, equiaxed grains has been perceived as a key strategy to solve the above-mentioned issues associated with AM processing.

In recent years, a wisdom originating from conventional casting practice, the so-called inoculation treatment, has been adopted in metal AM to achieve grain refinement [11,12]. The principle is to introduce a small amount of potent nucleant particles (externally added or formed in situ) into the melt to promote heterogeneous nucleation, achieving fine,

equiaxed grains. So far, the adaption of inoculation treatment has produced encouraging results in the AM of aluminum (Al) alloys [13–17]. Some of the inoculants (or grain refiners) developed in cast Al alloys, such as TiB_2 and hexaborides (e.g., LaB_6 , CeB_6 , and CaB_6), have been successfully adopted in AM to refine Al alloys [14,15,18–20]. In addition, new inoculants, such as the $\text{L}_{12}\text{-Al}_3\text{X}$ ($\text{X} = \text{Zr}, \text{Ti}, \text{Sc}, \text{Hf}, \text{or Ta}$) formers, have also been developed specifically for the rapid solidification conditions in AM [16,21,22]. These grain refiners not only improved the AM processability of a number of commercialized high-strength Al alloys (e.g., 2xxx, 6xxx, and 7xxx series Al alloys) but also helped to develop novel Al alloys and Al-based composites specifically suitable for AM processing to satisfy the ever-growing demand for weight reduction in the automobile and aerospace industries [17,23–25].

While a number of inoculants have been demonstrated to refine Al alloys during AM, their grain-refining efficiencies can vary significantly. For example, Liu et al. [26] reported the achievement of grain refinement in an AM-fabricated 7075 alloy after inoculation with TiC or TiH_2 nanoparticles. However, to achieve a complete columnar-to-equiaxed transition (CET) and a fully equiaxed microstructure in the alloy, the minimum required content of TiC (2 wt.%) was much higher than that of TiH_2 (0.8 wt.%), indicating a much higher efficiency of TiH_2 in refining Al upon AM. From the industrial application perspective, it is generally preferred to achieve complete CET at a minimized inoculation content so as to reduce cost and avoid inclusion. Hence, it is intriguing to investigate and understand the factors controlling the grain-refining efficiency of an inoculant and therefore to further reveal the grain-refining mechanisms at work during rapid AM solidification.

In metal casting, it is generally agreed that the efficiency of a grain refiner is predominantly determined by the atomic matching (or lattice registry, δ) between the grain refiner and the matrix crystal, which governs the interfacial energy between these two crystals [27,28]. A smaller atomic mismatch is associated with a higher refining efficiency. In addition to the interatomic matching, other factors such as the thermal stability, the distribution and formation incubation of the corresponding nucleant particle, and the solute effect provided by the inoculant can also significantly influence the refining efficiency [29–31]. Specifically, the incorporation of growth-restrictive solutes to promote heterogeneous nucleation via generating constitutional supercooling (CS) has long been considered an effective method to refine cast metals [11,12,32]. However, there exists a scarcity of research on the influence of solutes on the refining efficiency of inoculators in metal AM. The present work aims to deepen our understanding in this area by comparing the efficiency of two inoculants, LaB_6 and Ti, in refining Al during AM. The former is a typical externally added nucleant for Al refinement [15,33], whereas the latter is a typical $\text{L}_{12}\text{-Al}_3\text{X}$ former during AM of Al alloys (i.e., addition of Ti leads to the in situ formation of $\text{L}_{12}\text{-Al}_3\text{Ti}$ nucleant particles) [16,34]. Both LaB_6 and $\text{L}_{12}\text{-Al}_3\text{Ti}$ have been verified as effective nucleants to nucleate Al due to their extremely low δ with Al [15,16]. Furthermore, Ti is known as a growth-restrictive solute element in Al, effectively leading to grain refinement [11,30]. The 2024 Al alloy, a typical high-strength aeronautic Al alloy but with low AM processability, was selected as a demonstration platform for this work.

2. Experimental Methods

2.1. Powder Feedstock Preparation

Commercially gas-atomized 2024 Al alloy powder (size: 20–63 μm , composition: 3.70 wt.% Cu, 1.21 wt.% Mg, 0.40 wt.% Mn, 0.09 wt.% Si, 0.15 wt.% Fe, and the balance Al), sourced from LPW Technology, was used as the raw powder. Highly pure (99.9%) LaB_6 nanoparticles (ALB Materials Inc., Henderson, NV, USA), with an average size of 80 nm, and Ti nanoparticles (purity of 99%, SkySpring Nanomaterials Inc., Houston, TX, USA), with an average size of 60 nm, were used as the inoculants. Alloy powder feedstocks were prepared by mixing the 2024 alloy powder with the inoculant nanoparticles at three different inoculation content levels, i.e., 0.5 wt.%, 1 wt.%, and 2 wt.%, using the previously invented vibrative agitation method [15]. Figure 1 shows the morphologies of the nucleant nanoparticles, the 2024 alloy, and the inoculated 2024 alloy powders, examined using

scanning electron microscopy (SEM). Despite the presence of a few agglomerations, the majority of the nanoparticles were uniformly dispersed on the surfaces of the 2024 alloy powder particles after the vibrative agitation.

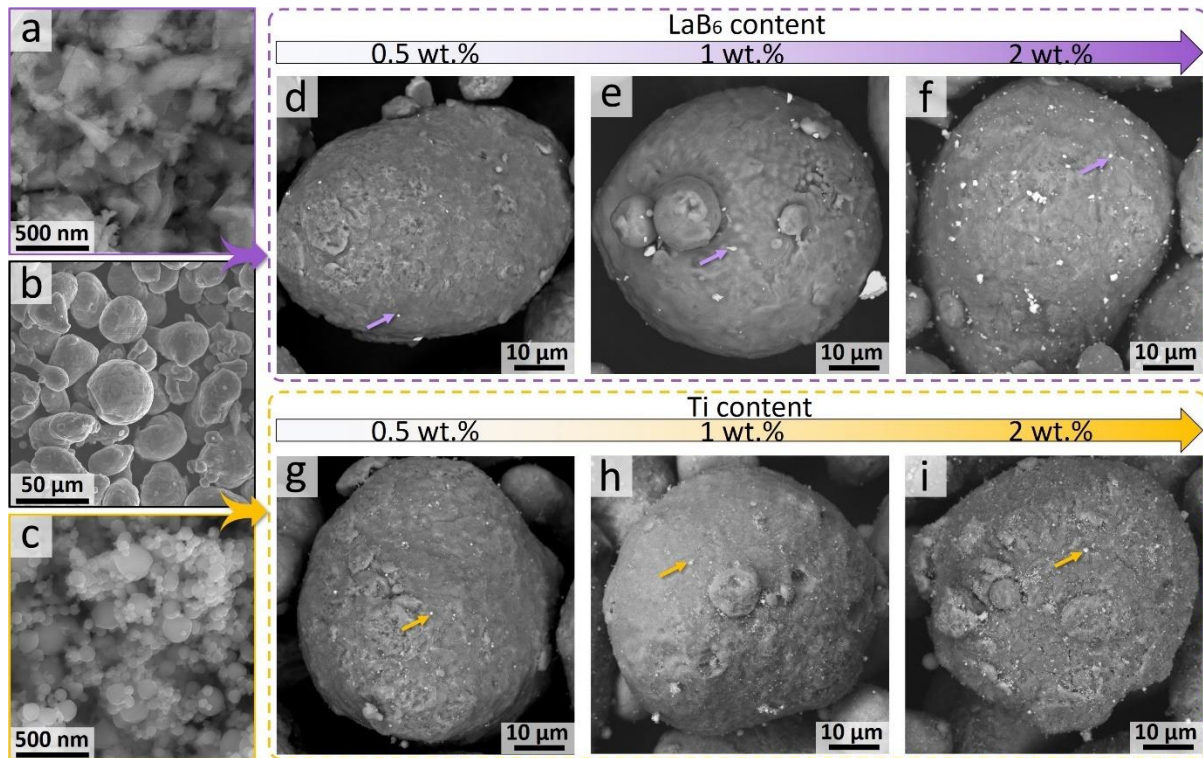


Figure 1. SEM images of (a) LaB_6 nanoparticles, (b) 2024 Al alloy powder particles, (c) Ti nanoparticles, (f–i) typical single-, (d–f) LaB_6 -inoculated-, and (g–i) Ti-inoculated 2024 alloy powder particles with different inoculation contents of (d,g) 0.5 wt.%, (e,h) 1 wt.%, and (f,i) 2 wt.%, with arrows in (d–i) indicating the nanoparticles.

2.2. AM Processing

Both the 2024 Al alloy and the inoculated 2024 alloys (termed as 2024, 2024-0.5 LaB_6 , 2024-1 LaB_6 , 2024-2 LaB_6 , 2024-0.5Ti, 2024-1Ti, and 2024-2Ti) were fabricated using an SLM125HL powder bed fusion system (SLM Solutions Group AG), with a laser spot diameter of 80 μm . Then, 10 mm \times 10 mm \times 10 mm cubic samples were built onto a pure Al platform preheated to 200 $^\circ\text{C}$ with the processing parameters listed in Table 1. Note that this processing parameter set was optimized for 2024 Al alloy as per our previous work [4]. Although the inoculated alloy may possess a different optimized parameter set due to the compositional difference, the same processing parameter set was used herein to ensure the consistency of the melting condition. For each alloy, at least three samples were fabricated to ensure the reproducibility of microstructural characterization.

Table 1. Optimized AM processing parameters.

Process Parameter	Value/Pattern
Laser power	375 W
Scanning speed	1200 mm/s
Hatching spacing	130 μm
Layer thickness	30 μm
Preheating temperature	200 $^\circ\text{C}$
Rotation angle between adjacent layers	67 $^\circ$
Scanning strategy	Zigzag scan pattern

2.3. Microstructural Characterization

A Reichert-Jung POLYVAR MET optical microscope was employed to examine the densification of the AM-fabricated alloys. The porosity and crack fraction of the AM-fabricated alloys were examined through image analysis using the ImageJ software as per the procedure outlined in [34]. For each alloy, four cross-sectional micrographs were analyzed to ensure reproducibility. A JOEL 7800 field emission scanning electron microscope (FESEM), equipped with electron backscattered diffraction (EBSD) and energy dispersive spectroscopy (EDS) detectors, was utilized to characterize the morphology of the feedstock powders and microstructures of the AM-fabricated alloys. Samples for microstructure characterization were cut from the AM-fabricated alloys along their longitudinal direction, i.e., the building direction (BD), followed by mechanically grinding and polishing following standard metallographic procedure. Keller's reagent, composed of 5 mL HNO₃, 3 mL HCl, 2 mL HF, and 190 mL H₂O, was employed to etch the samples for 5 s and reveal their microstructures. EBSD inverse pole figure (IPF) mapping was performed with a scanning step of 0.2 μm, and a critical misorientation angle of 10° was used to identify grain boundaries. For composition analysis, EDS point scans were conducted with a low current of 0.5 nA to minimize the interaction region created by the electron beam and enhance the accuracy of determinations.

Microstructures of the 2024-2LaB₆ and 2024-2Ti alloys were further examined using an Hitachi HF5000 transmission electron microscope (TEM), equipped with dual EDS detectors and operated at an acceleration voltage of 200 kV. The overlapped selected area electron diffraction (SAED) technique was utilized to determine the orientation relationship (OR) between the nucleant particle and the adjacent aluminum grain. High-resolution TEM images were post-processed using inverse fast Fourier transforming (IFFT) with Gatan DigitalMicrograph™ software to reduce noise. TEM samples were prepared using an FEI Dual FIB/SEM-SCIOS focused ion beam (FIB) milling system.

3. Results

3.1. Densification

Figure 1 shows the densification behavior of the AM-fabricated 2024 and inoculated 2024 alloys. Similar to the AM-fabricated high-strength Al alloys reported previously [4,13,35], the present 2024 alloy featured a high fraction of cracks (~1.81%) parallel to the BD. These cracks possess lengths ranging from several hundreds of micron meters to several millimeters, spanning across multiple layers or even the entire sample. As shown in Figure 2b–d, inoculation with LaB₆ nanoparticles provides a marginal influence on the crack density (from ~1.81% to ~1.54%) but led to a higher porosity within the alloy, particularly at a high addition level (e.g., 2 wt.% LaB₆ with a porosity of ~1.49%).

In contrast, inoculation with Ti nanoparticles effectively alleviated cracking in the 2024 alloy upon AM processing. Addition of 0.5 wt.% Ti nanoparticles significantly reduced the crack length and fraction (~1.04%) in the 2024-0.5Ti alloy (Figure 2e). Increasing the Ti content to 1 wt.% led to a more pronounced cracking alleviation. As demonstrated in Figure 2f, the 2024-1Ti alloy was crack-free with only a small fraction of spherical pores (~0.57%) being observed. These pores were considered as gas pores that were commonly observed in AM-fabricated metals [1]. Similar to the LaB₆ inoculation, further increasing the Ti content to 2 wt.% resulted in a higher porosity (~0.99%) in the 2024-2Ti alloy (Figure 2g). This could be attributed to the reduced powder fluidity caused by the higher inoculation content of nanoparticles. A similar phenomenon has also been reported in other AM-fabricated metals with inoculation treatments [36,37]. This result indicates that compared with LaB₆, inoculation with Ti nanoparticles has a significantly higher efficiency in eliminating cracking of the 2024 alloy upon AM processing.

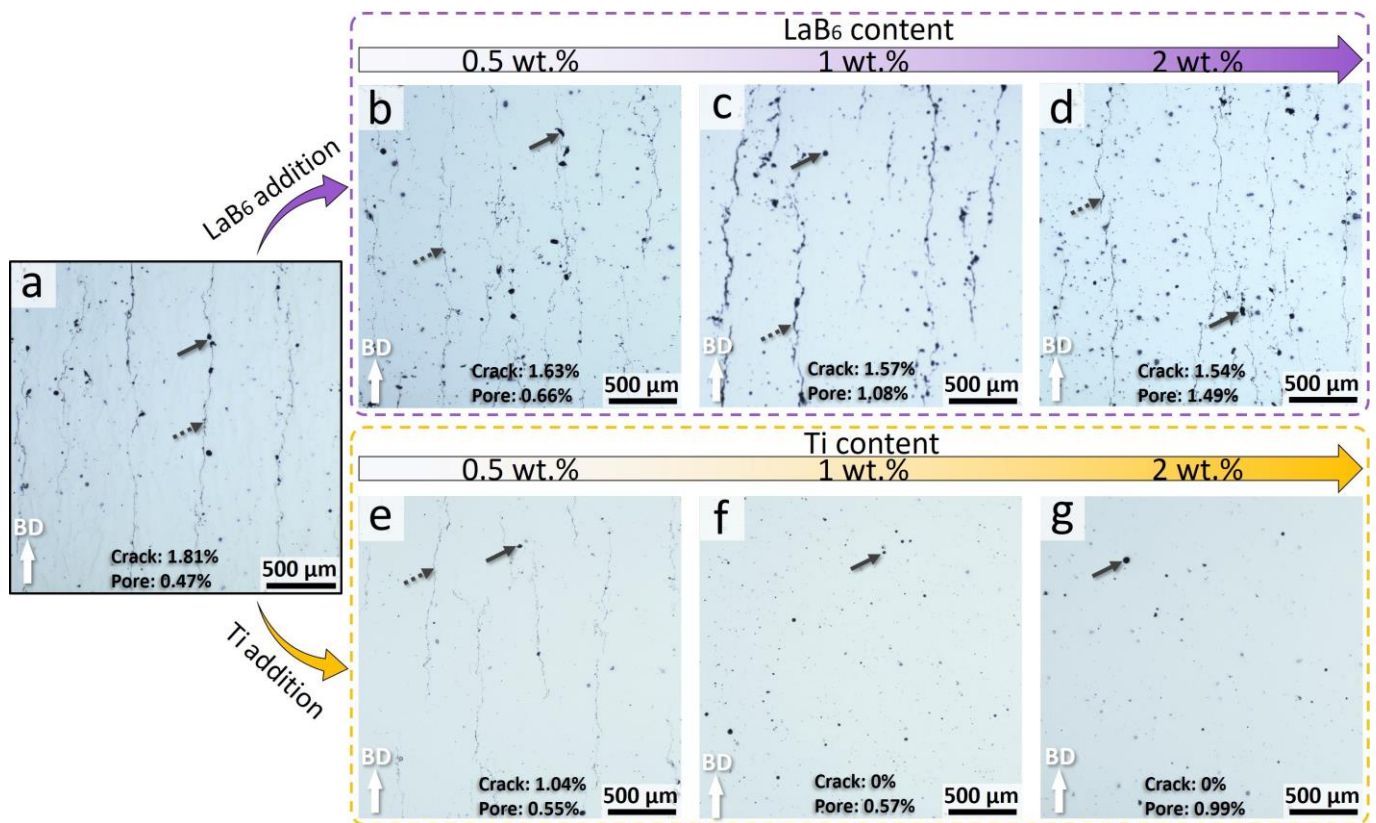


Figure 2. Longitudinal optical micrographs of the AM-fabricated (a) 2024 alloy, (b) 2024-0.5LaB₆ alloy, (c) 2024-1LaB₆ alloy, (d) 2024-2LaB₆ alloy, (e) 2024-0.5Ti alloy, (f) 2024-1Ti alloy, and (g) 2024-2Ti alloy. The cracks and pores are pointed to by the dashed arrows and solid arrows, respectively. Statistical analysis data are also enclosed to show the fractions of the cracks and pores within the alloys.

3.2. Grain Morphology Evolution

Figure 3 depicts the EBSD-IPF maps and the corresponding pole figures of all the AM-fabricated alloys on their longitudinal cross-sections. As depicted in Figure 3a, the AM-fabricated 2024 alloy is featured with large, columnar grains with widths ranging from 20–60 μm and lengths up to hundreds of micron meters. The IPF color code indicates that the majority of these columnar grains have their <100> orientations parallel to the BD, leading to a strong <100> texture in the alloy along the BD as shown in Figure 3h1. Cracks can be clearly observed in between these columnar grains, consistent with previous works on the AM of high-strength Al alloys [38,39]. This indicates that the intergranular region is particularly vulnerable to the thermal stresses caused by rapid cooling and solidification shrinkage, which exemplified a typical hot-cracking feature widely reported in AM-fabricated high-strength Al alloys [13,38,39].

The incorporation of LaB₆ provides limited refinement to the 2024 alloy upon AM processing. As shown in Figure 3b,c, addition to LaB₆ from 0.5 wt.% to 1 wt.% only slightly reduced the size of the columnar grains, whereas almost no CET can be observed in both the 2024-0.5LaB₆ and 2024-1LaB₆ alloys. Although further increasing the LaB₆ content to 2 wt.% led to the formation of a small fraction of equiaxed grains, the microstructure was still dominated by the large, textured, columnar grains. Thus, similar to the 2024 alloy, the LaB₆-inoculated 2024 alloys possessed pronounced <100> textures as illustrated in Figure 3h2–4. Furthermore, hot-cracking can be observed to propagate along the intergranular regions, spanning over multiple columnar grains. This result was contrary to the previous works on the AM-fabricated AlSi10Mg alloy [15,33], where inoculation with a small amount of LaB₆ nanoparticles led to a significant grain refinement. Detailed discussion will be provided in Section 4.2.

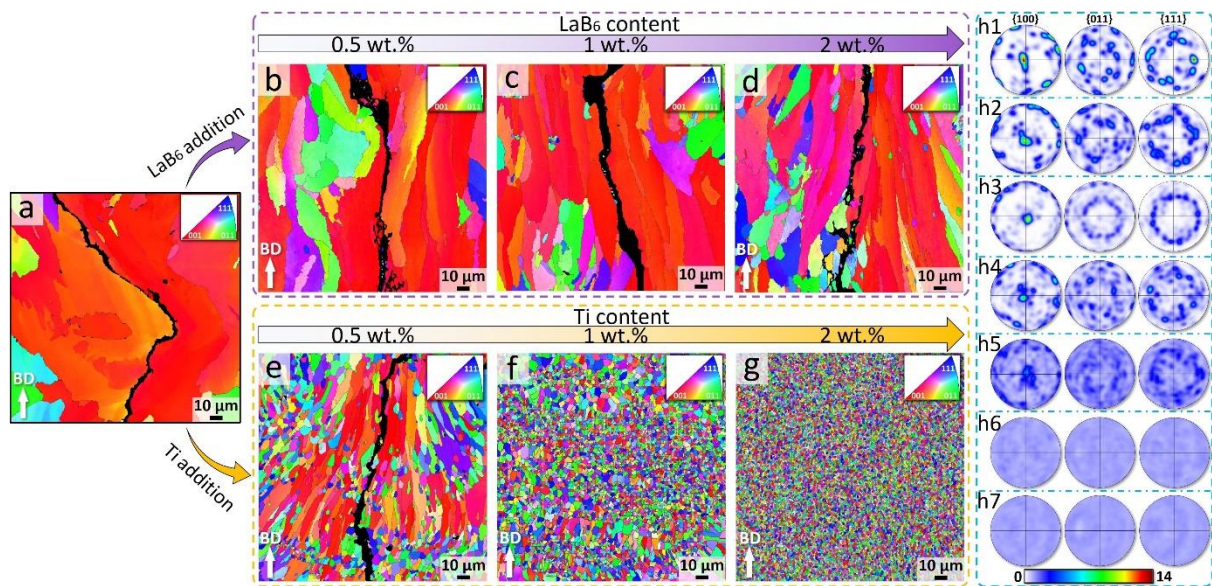


Figure 3. Longitudinal EBSD-IPF grain orientation maps (a–g) and the corresponding pole figures (h1–h7) of the AM-fabricated alloys: (a,h1) 2024 alloy, (b,h2) 2024-0.5LaB₆ alloy, (c,h3) 2024-1LaB₆ alloy, (d,h4) 2024-0.5LaB₆ alloy, (e, h5) 2024-0.5Ti alloy, (f,h6) 2024-1Ti alloy, and (g,h7) 2024-2Ti alloy. The crystal orientations in the IPF maps were viewed along the BD. The color scale in the pole figures indicates the relative intensity of the diffraction peaks.

In comparison, inoculation treatment with Ti nanoparticles effectively refined the grains and led to CET in the AM-fabricated 2024 alloys. As shown in Figure 3e, the addition of 0.5 wt.% Ti nanoparticles not only significantly reduced the size of columnar grains but also led to the formation of some fine, equiaxed grains interspersed among the columnar grains. Compared to the textured columnar grains, these equiaxed grains were randomly oriented, leading to a reduced texture in the 2024-0.5Ti alloy, as presented in Figure 3h5. Nevertheless, due to the existence of columnar grains, hot-cracking cannot be eliminated in the alloy. Increasing the Ti content to 1 wt.% led to substantial grain refinement and achieved complete CET in the 2024-1Ti alloy. The complete elimination of columnar grains led to a texture-free microstructure of the alloy, as shown in Figure 3h6. Statistical analysis shows that the majority of these equiaxed grains had a grain size less than 5 μm , corresponding to the average grain size of 2.8 μm in the 2024-1Ti alloy. Further increasing the Ti content to 2 wt.% led to a more pronounced refinement to the equiaxed grains and a more uniform microstructure in the 2024-2Ti alloy (Figure 3g). The size of the equiaxed grains ranges from 0.7 μm to 3 μm , which corresponds to the average grain size of 1.5 μm of the alloy. This result signifies that the Ti inoculation possesses significantly higher efficiency than the LaB₆ inoculation in refining Al grains during the AM of the 2024 alloy.

3.3. Microstructural Characterization

To investigate the distribution of the inoculant nanoparticles, microstructural characterization was further conducted using SEM on the 2024-2LaB₆ alloy, 2024-0.5Ti alloy and 2024-1Ti alloy. As shown in Figure 4a–c, both alloys possess fine intermetallic particles with an average size of ~ 200 nm interspersed in between the Al dendrites. These intermetallic phases are possibly the Al₂Cu or Al₂CuMg phases widely reported in AM-fabricated 2xxx series alloys [40,41]. In the 2024-2LaB₆ alloy, numerous LaB₆ nanoparticles (bright phase, indicated by the arrows) were uniformly distributed in the Al grain, as confirmed by the EDS mapping shown in Figure 4g. The EDS quantitative analysis (operated at a low current) further demonstrated the absence of La and B solutes within the Al dendrites, which demonstrates the high stability of LaB₆ nanoparticles upon AM processing. Given

the marginal refining response of the 2024-2LaB₆ alloy, it is speculated that the inoculated LaB₆ nanoparticles did not serve as the nucleant particles.

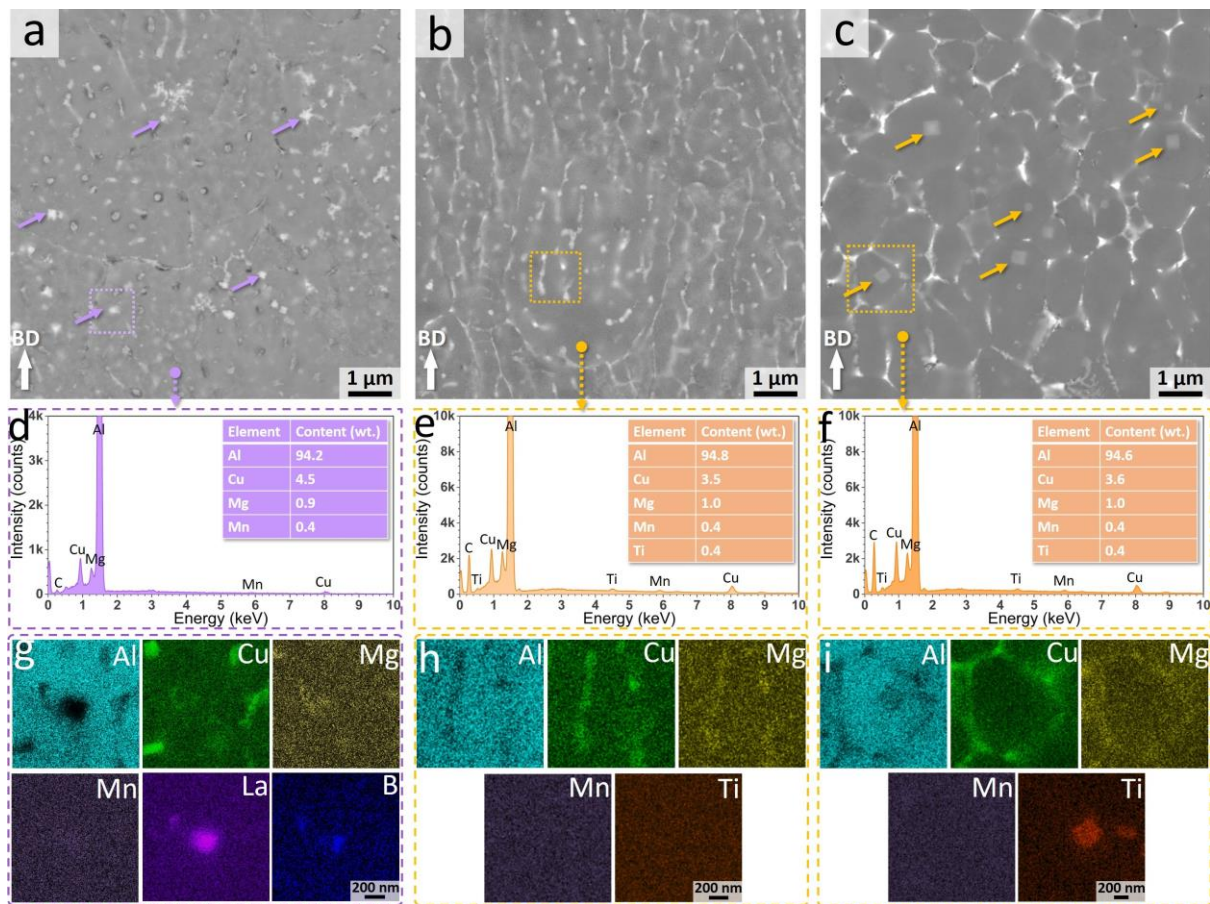


Figure 4. Longitudinal SEM-backscattered electron images (a–c), the representative EDS spectra (d–f) of the point analyses on the Al matrix, and the corresponding EDS maps (g–i) of the marked areas of (a,d,g) 2024-2LaB₆, (b,e,h) 2024-0.5Ti, and (c,f,i) 2024-1Ti, with the insets in (d–f) showing the solute concentrations. The solid arrows in (a) and (c) indicate the LaB₆ and Al₃Ti nanoparticles, respectively.

For the 2024-0.5Ti alloy, the microstructure only consists of Al dendrites and the Cu-rich intermetallic phase particles, wherein no Ti-containing particles were detected. The EDS quantitative analysis reveals that Al dendrites contain Ti solute at approximately 0.4 wt.%. This indicates that almost all the inoculated Ti nanoparticles exist in the form of solute in the α -Al grains. In the previous works on Ti-inoculated Al alloys, the substantial grain refinement was ascribed to the in situ formation of Al₃Ti nucleant particles that promoted the heterogeneous nucleation of Al grains [16,30,40,42,43]. Thus, the absence of such nucleant particles in the 2024-0.5Ti alloy could be responsible for the insufficient grain refinement as presented in Figure 3e. Further increasing the Ti content to 1 wt.% led to the formation of numerous cuboidal particles (50–200 nm in size, indicated by the arrows) within the Al dendrites, as presented in Figure 4c. The EDS mapping shown in Figure 4i demonstrates these particles being enriched with Ti. According to the previous works on AM-fabricated Al alloys with Ti inoculation [16,34], these particles are considered as an Al₃Ti phase attributed to the peritectic reaction between Al and Ti. Because the majority of these Al₃Ti nanoparticles were identified within the Al grains, they were considered to serve as nucleant particles to nucleate Al grains upon solidification. Furthermore, the 2024-1Ti alloy had a Ti solute (0.4 wt.%) similar to the 2024-0.5Ti alloy (Figure 4f). This suggests that there is a threshold inoculation content of Ti at ~0.4 wt.%, over which the Al₃Ti nucleant particles can form in situ. Note that the microstructures of other alloys,

namely the 2024-0.5LaB₆, 2024-1LaB₆, and 2024-2Ti alloys, are similar to the 2024-2LaB₆ and 2024-1Ti presented in Figure 4, except for the higher fractions of nanoparticles in the alloys with higher inoculation concentrations. Thus, these microstructures are not presented herein for the sake of brevity.

To further investigate the orientation relationships (ORs) between the nanoparticles and the Al grains and to understand the grain refinement mechanisms, TEM microstructural examination was conducted on the 2024-2LaB₆ and 2024-1Ti alloys. Figure 5a,b show a representative bright-field TEM micrograph and corresponding EDS spectrum of the 2024-2LaB₆ alloy, showing an LaB₆ nanoparticle located at an Al-grain center. Considerable overlapped SAED measurements have confirmed that there was no reproducible OR between the LaB₆ nanoparticles and the Al matrix, as exemplified by Figure 5c. This can also be confirmed by the bright-field image after sample tilting to the [001]_{Al} zone axis (inset in Figure 5a). The Al matrix appears dark due to a pronounced diffraction effect, while the LaB₆ nanoparticle exhibits a comparatively brighter appearance, suggesting that the electron beam is not aligned with any specific zone axis of the nanoparticle. This indicates that the LaB₆ nanoparticles did not act as nucleants to nucleate Al grains. Although the two-dimensional cross-sectional image may not reveal all the LaB₆ nanoparticles embedded within the Al grain, the extensive epitaxial grain growth observed in the 2024-2LaB₆ alloy suggests the lack of heterogeneous nucleation on the LaB₆ nanoparticles.

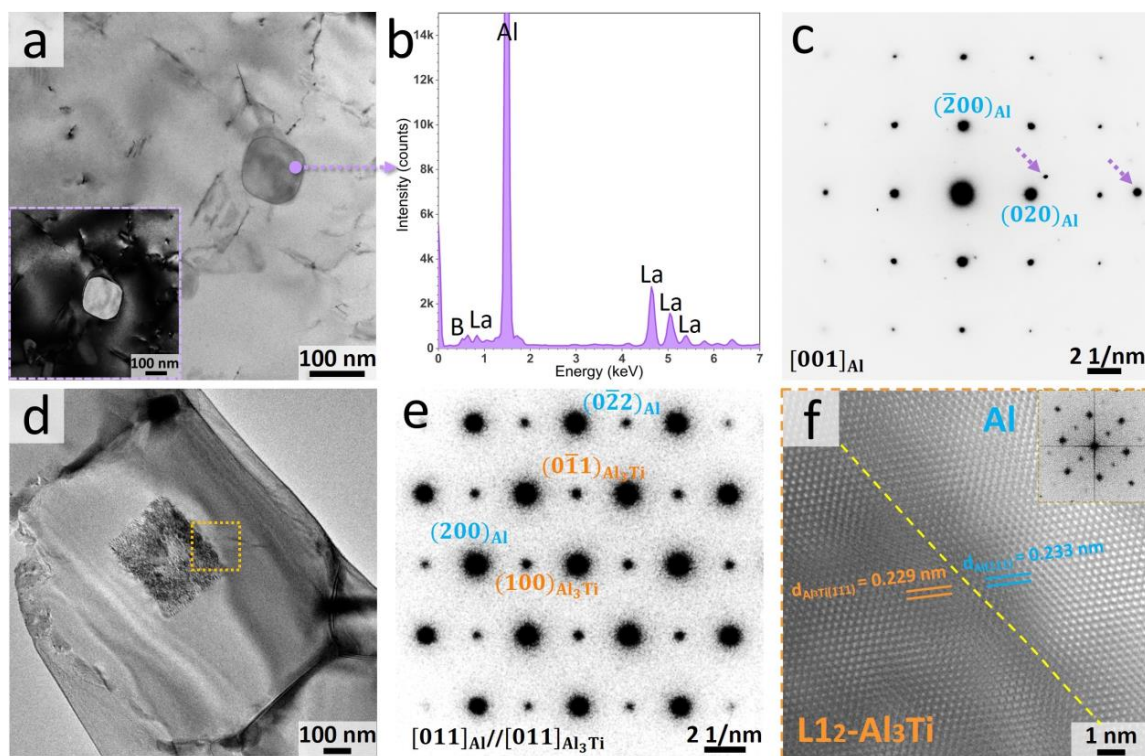


Figure 5. (a) Bright-field TEM micrograph of the 2024-2LaB₆ alloy, with the inset showing the micrograph after sample tilting to the [001]_{Al} zone axis, (b) the corresponding EDS spectrum (acquired in STEM mode), and (c) SAED pattern taken at the Al/LaB₆ interface along the [001]_{Al} zone axis after sample tilting; (d) bright-field TEM micrograph of the 2024-1Ti alloy, (e) the corresponding SAED pattern taken at the Al/L1₂-Al₃Ti interface along the [011]_{Al} zone axis after sample tilting, and (f) the high-resolution TEM image of the area marked in (d), showing the coherent interface between these two crystals. Note that the diffraction spots of the LaB₆ nanoparticle, indicated by the dashed arrows in (c), are obtained, but they cannot be indexed because the incident electron beam is away from any zone axis of the LaB₆.

In contrast, the SAED pattern shown in Figure 5d demonstrates the typical cube-on-cube relationship between the Al grain and the Al₃Ti nanoparticle in the 2024-1Ti alloy. In

addition, the existence of the (100) and (110) type superlattice reflections confirms the $L1_2$ ordered structure of the Al_3Ti phase (i.e., $L1_2-Al_3Ti$). Because this crystallographic OR was repeatedly identified across the $Al/L1_2-Al_3Ti$ interfaces in 2024-1Ti, this can be considered to be a specific and well-defined OR as follows:

$$[011]_{Al} \parallel [011]_{L1_2-Al_3Ti}, (022)_{Al} \parallel (022)_{L1_2-Al_3Ti} \text{ (OR1)}$$

The high-resolution TEM micrograph and the corresponding fast Fourier transforming (FFT) pattern (Figure 5e) taken along the $[011]_{Al}$ axis evidence the highly coherent interface between the $L1_2-Al_3Ti$ nanoparticle and the Al matrix, which is consistent with previous works on AM-fabricated Ti-containing Al alloys [34,40,42,43]. This evidences the occurrence of heterogeneous nucleation of $\alpha-Al$ on the nanoparticles.

4. Discussion

It is demonstrated from Figure 3a that the AM-fabricated 2024 Al alloy possesses coarse columnar grains. This is attributed to the directional solidification nature of melt pools [2,3,5]. Inoculation treatment with LaB_6 and Ti nanoparticles exhibited significantly different grain refining efficiencies in this alloy upon AM processing. The former provided almost no refining effect to the alloy (Figure 3b–d), whereas the latter possessed a high refining efficiency (Figure 3e–g), and a complete CET can be obtained at the inoculation content of 1 wt.% Ti (Figure 3f). The difference in their refining efficiencies is discussed in the following sections.

4.1. Nucleation Conditions

As per the Winegard and Chalmers nucleation theory [44], the Interdependence theory [45], and the recently proposed numerical nucleation model by Xu et al. [46], the successful initiation of heterogeneous nucleation and the achievement of CET requires the generation of sufficient undercooling (ΔT) in front of the growing solid/liquid S/L interface to surpass the critical nucleation undercooling (ΔT_n) required for heterogeneous nucleation (i.e., $\Delta T \geq \Delta T_n$). Hence, ΔT and ΔT_n are two key factors that determine the grain morphology and size of the solidified metal. An equiaxed-grain microstructure with fine grain size is favored with a large ΔT and a small ΔT_n .

As initially proposed by Turnbull and Vonnegut [27] and experimentally verified recently by Wang et al. [47,48] and Fan et al. [49,50], ΔT_n is closely related to the interatomic mismatch (designated as lattice discrepancy, δ) between the nucleant particle and the growing metal, expressed by the following equation:

$$\Delta T_n = \frac{c_E}{\Delta S_V} \delta^2 \quad (1)$$

where c_E represents the coefficients of elasticity and ΔS_V denotes the entropy of phase transition per volume.

In cases of rapid solidification of an alloy, the ΔT , defined as the difference between the melt temperature (T_M) and the alloy liquidus temperature (T_L), can be approximated as the sum of two types of undercooling: thermal undercooling (ΔT_t) and constitutional supercooling (ΔT_{CS}) [51]. The ΔT_t is closely related to the lag in the actual growth rate of the S/L interface compared to the theoretical pull rate induced by the cooling rate in the melt [52]. Factors such as increased viscosity, decreased mobility, and nucleation density can slow down the actual growth rate, causing the liquid ahead of the S/L interface to remain supercooled with a temperature below its theoretical freezing point, generating ΔT_t . Thus, ΔT_t is influenced by (i) the cooling rate, which can be controlled through processing parameter manipulation (e.g., laser power and scan speed in AM processing) and (ii) the actual growth rate of the S/L interface, which is affected by the solute rejection from the growing solid to the liquid. Solutes with a low solubility and a slower diffusion rate may possess a higher tendency to delay the dendrite growth and thus enable a larger ΔT_t in

front of the S/L interface [53]. In terms of ΔT_{CS} , it is also closely related to the solute segregation ahead of the S/L interface [45,51]. Due to the different solubilities in the solid and the liquid, excess solute atoms that cannot dissolve in the solid are rejected towards the adjacent liquid, causing a pile-up of solute ahead of the growing S/L interface. This alters the solidification temperature at the S/L interface in combination with the thermal gradient, creating ΔT_{CS} [52]. The efficiency of a solute to generate ΔT_{CS} is quantitatively expressed by the growth restriction factor, known as Q , expressed as follows [11]:

$$Q = m(k - 1)C_0 \quad (2)$$

For an alloy with multiple solute elements, the Q value can be approximated by

$$Q = \sum m(k - 1)C_0 \quad (3)$$

where k is the partition coefficient, m is the slope of the liquidus (assumed to be the straight line), and C_0 denotes the solute concentration. Solute with a large Q value can more rapidly generate ΔT_{CS} ahead of the S/L interface, promoting heterogeneous nucleation.

4.2. The Importance of Solute

In the present 2024 alloy, the predominant solutes are Cu (3.70 wt.%) and Mg (1.2 wt.%), which are weak growth-restrictive solutes in Al, corresponding to a relatively small Q value of ~15 K of the alloy as shown in Table 2. Moreover, rapid AM solidification is associated with an extremely large thermal gradient, typically ranging from 10^5 to 10^7 K/m [1]. Such a steep thermal gradient further restricts the constitutional supercooling zone and thus the ΔT_{CS} [2,5,53–55]. In addition, both Cu and Mg possess a low segregation tendency, due to their large solubilities in Al (≥ 6 wt.%), which in turn limits the generation of ΔT_i . Thus, a relatively small ΔT is expected at the front of the S/L interface during AM of the 2024 alloy. On the other hand, for alloy solidification without inoculation treatment, heterogeneous nucleation occurs on native nucleants in the melt such as impurities and oxides. In general, these native nucleants possess a relatively large δ with the metal matrix and thereby a relatively large ΔT_n [53]. As a result, the overall ΔT is insufficient to surpass the ΔT_n for activating heterogeneous nucleation in the 2024 alloy, as schematically illustrated in Figure 6a. The lack of heterogeneous nucleation ahead of the growing S/L interface favored the growth of columnar grains along the thermal gradient direction (i.e., BD). When the subsequent layer is built, the solidification occurred through direct epitaxial growth from the grains of the previous layer due to the low nucleation barrier, eventually forming extensively coarse, textured, columnar grains spanning over multiple layers as shown in Figure 3a. During solidification, the formation of such large columnar grains is associated with fragile intergranular liquid channels, which were prone to deformation and rupture due to thermal stress [56], leading to high fractions of cracks, as shown in Figure 2a.

Table 2. The k , m , and $m(k - 1)$ values of some solute elements in Al [11], the nucleant particle type, and the calculated Q values of 2024, 2024-2LaB₆, 2024-0.5Ti, 2024-1Ti, and AlSi10Mg alloys [15].

Element/Alloy	k	m	$m(k-1)$	Q	Nucleant
Cu	0.17	−3.4	2.8	-	-
Mg	0.51	−6.2	3	-	-
Mn	0.94	−1.6	1.9	-	-
Ti	9	30.7	245.6	-	-
Si	0.11	−6.6	5.9	-	-
2024 alloy	-	-	-	15 K	Native
2024-2LaB ₆	-	-	-	15 K	LaB ₆
2024-0.5Ti alloy	-	-	-	90 K	Native
2024-1Ti alloy	-	-	-	90 K	L1 ₂ -Al ₃ Ti
LaB ₆ -inoculated AlSi10Mg [15]	-	-	-	61 K	LaB ₆

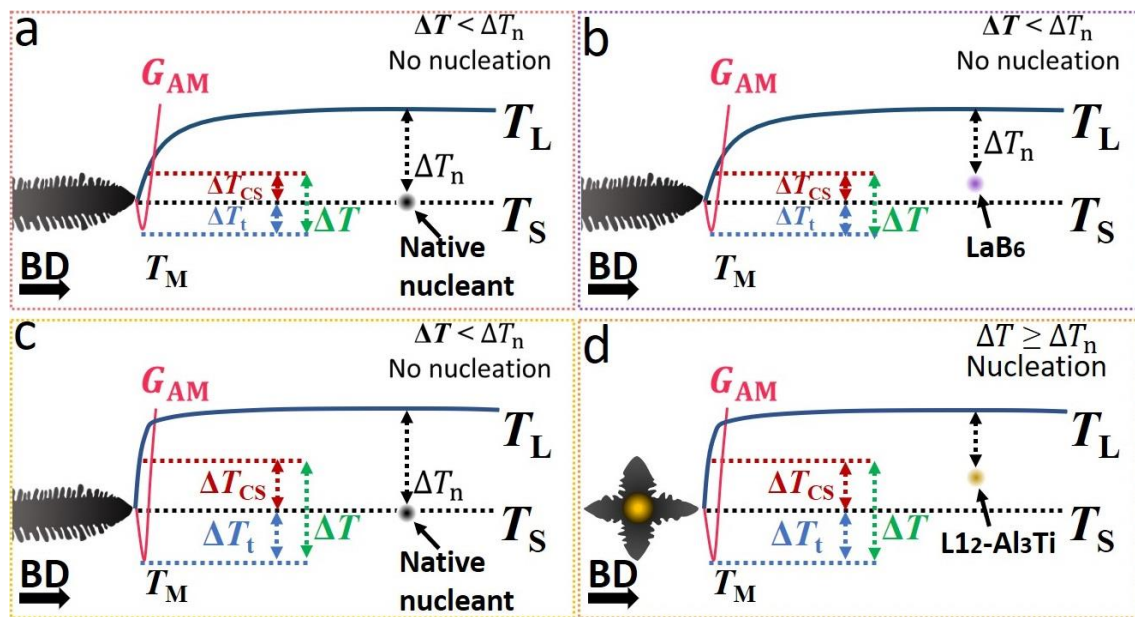


Figure 6. Schematic illustrations of the generation of ΔT_{CS} and ΔT_t ahead of the growing S/L interface and the critical nucleation undercooling ΔT_n in (a) 2024 alloy, (b) 2024-2LaB₆ alloy, (c) 2024-0.5Ti, and (d) 2024-1Ti alloy, where G_{AM} represents the thermal gradients; T_S , T_L , and T_M denote the solidus temperature, liquidus temperature, and melt temperature, respectively.

Inoculation with LaB₆ nanoparticles, even up to 2 wt.%, provided marginal refinement to the 2024 alloy (Figure 3b–d). According to previous studies [15], LaB₆ is an effective nucleant for Al due to the extremely small δ ($\delta = 2.14\%$) with Al and thus the significantly reduced ΔT_n for Al nucleation. The ineffectiveness of LaB₆ in the present 2024 alloy indicates that despite the reduction in ΔT_n , the solute-driven ΔT ahead of the S/L interface was too small to surpass the ΔT_n . Therefore, heterogeneous nucleation cannot be activated, as illustrated in Figure 6b. Upon solidification, these LaB₆ nanoparticles were either pushed towards the grain/dendrite boundaries or engulfed by the growing grain, processing random ORs with the Al matrix, as demonstrated in Figure 5b. Unlike the 2024 alloy, our previous work [33] demonstrated that a small addition of LaB₆ (0.2–0.5 wt.%) was effective in achieving CET in the AM-fabricated AlSi10Mg alloy. Such a contradiction can be understood by the significant solute contribution in the AlSi10Mg alloy. This alloy commonly contains ~10 wt.% Si and ~0.45 wt.% Mg, which corresponds to a Q value of ~61 K, much greater than the 2024 alloy. Furthermore, the Si content in the alloy is significantly greater than its corresponding equilibrium solubility (~1.55 wt.%), signifying a strong segregation tendency upon solidification and thus a large ΔT_t to be generated. Thus, in the AlSi10Mg alloy, a much higher ΔT is expected at the growing S/L interface to activate heterogeneous nucleation on LaB₆ nanoparticles, achieving grain refinement.

Unlike LaB₆, Ti inoculation provided pronounced refinement to the 2024 alloy, as shown in Figure 3e–g. This resulted from the synergy between the solute and the nucleant particles. Ti is known as one of the most effective growth restriction solutes in Al with high k and m values of 9 and 30.7, respectively [11]. As demonstrated in Figure 4e,f, the maximum dissolvable Ti solute is ~0.4 wt.% in the 2024 alloy during AM, which significantly increased the Q value of the alloy from 15 K to 90 K (Table 2). In addition, the segregation of Ti solute may also contribute to the growth lag of the Al dendrite and thereby the generation of ΔT_t ahead of the S/L interface. Thus, a much greater ΔT is expected at the growing S/L interface during the AM of Ti-containing Al alloys. In the present 2024-0.5Ti alloy, almost all the inoculated Ti existed as solute, whereas almost no extra nucleant particle was introduced. As such, the grain refinement is predominantly attributed to the solute effect caused by Ti. However, because of the lack of effective nucleant particles in the alloy (Figure 4b),

heterogeneous nucleation can only occur on native nucleants, which are associated with a large ΔT_t and small fraction. This significantly restricted the grain refinement efficiency despite the increase in ΔT , as schematically shown in Figure 6c. Thus, although there was a reduction in the overall grain size, the columnar structure and hot-cracking persisted in the alloy as shown in Figures 2b and 3b.

However, at a Ti content higher than 0.4 wt.%, the excess Ti can react in situ with Al to form the L_{12} - Al_3Ti nanoparticles, as demonstrated in Figure 4c,i. Similar to LaB_6 , L_{12} - Al_3Ti is also an effective nucleant for Al because of the extremely small δ ($\delta < 1\%$) across the Al/ L_{12} - Al_3Ti interface [16]. Thus, in addition to the increase in ΔT by the Ti solute, there was a significant reduction in the critical nucleation undercooling ΔT_n during AM of the 2024-1Ti alloy. Such a solidification condition guaranteed the much “easier” heterogeneous nucleation on the L_{12} - Al_3Ti nanoparticles (i.e., to satisfy $\Delta T \geq \Delta T_n$), schematically depicted in Figure 6d. As a result, complete CET and an equiaxed microstructure were achieved, as shown in Figure 3f. Compared to the columnar grains, the fine, equiaxed grains are more ready to accommodate thermal stress upon rapid solidification [13] so that a crack-free microstructure can be obtained, as shown in Figure 2f. Further increasing the Ti content to 2 wt.% produced a larger number of L_{12} - Al_3Ti nanoparticles throughout the melt pools, which ensures vaster nucleation events to occur, resulting in much finer grains in the 2024-2Ti alloy as presented in Figure 3g.

As aforementioned, AM is associated with a significantly large thermal gradient, which significantly limits the ΔT ahead of the growing S/L interface. Under this solidification condition, the addition of appropriate solutes to generate sufficient ΔT , and thereby to counteract the effect of the thermal gradient, is the prerequisite for the activation of heterogeneous nucleation. This has been demonstrated in previous works [53] where the inoculated nucleant particles can be activated only in the alloys with sufficient growth-restrictive solutes. In the present work, Ti inoculation not only introduced nucleant particles but also provided a solute effect in the alloy, which is the main reason for its superior refining efficiency compared to LaB_6 . The formation of those nanoparticles requires a Ti content higher than a critical content, which is approximately 0.4 wt.% in the present 2024 alloy. Note that this critical content may be closely related to the solidification thermodynamic, which can vary with different alloy systems and AM processing parameters. For example, Li et al. [57] inoculated 1 wt.% Ti in an AM-fabricated 2219 Al alloy and reported that almost all the inoculated Ti existed in the form of solute whilst no L_{12} - Al_3Ti was observed in the alloy. Although significant grain refinement was achieved in the alloy due to the growth restriction effect supplied by Ti, complete CET cannot be attained due to the lack of nucleant particles.

Hence, the implementation of inoculators that concurrently involve contributions from nucleant particles and solute is strongly advocated to attain a finely-grained, equiaxed microstructure during AM processing. Typical effective inoculators can be Al_3X ($X = Ti, Zr, Ta, V, Nb, Hf$) formers like Ti, Ta, V, and Hf. These inoculators are also growth-restrictive solutes in Al [11] and have been demonstrated effective in refining Al during conventional casting [30,58] and AM [21,31,59–61]. In addition to the present 2024 alloy, this strategy may also be applicable in other Al alloys to achieve CET, particularly those having insufficient growth-effective solutes and low Q values, e.g., 6061 ($Q_{6061} = \sim 7$ K) and 7075 ($Q_{7075} = \sim 16$ K) alloys [11].

5. Conclusions

The present work demonstrates the important role of solutes in achieving grain refinement during AM by comparing the refining efficiencies of LaB_6 nanoparticle and Ti nanoparticle inoculants in 2024 Al alloy during AM processing. Based on the results, the following conclusions can be made:

- i. Inoculation with LaB_6 nanoparticles, even up to 2 wt.%, provided marginal grain refinement in the AM-fabricated 2024 alloy. A random orientation relation was

- found across the Al/LaB₆ interfaces, which indicates that LaB₆ cannot nucleate Al grains upon AM solidification.
- ii. The ineffectiveness of LaB₆ was attributed to the insufficient growth-restrictive solute in the 2024 alloy. Thus, despite the reduction in ΔT_n , the solute-driven ΔT ahead of the S/L interface was too small to surpass it, leading to insufficient nucleation events.
 - iii. Compared to LaB₆, inoculation with Ti provided more pronounced grain refinement in the 2024 alloy, and a complete CET was achieved at a Ti content greater than 1 wt.%.
 - iv. The higher grain-refining efficiency of Ti inoculation can be well understood by the synergy between the solute and the nucleant particles. The dissolved Ti solute significantly increased the overall ΔT ahead of the S/L interface through the growth-restrictive effect on the alloy, whilst the excess Ti led to the in situ formation of L1₂-Al₃Ti nanoparticles, which act as effective nucleant particles to reduce the ΔT_n for Al nucleation. As a result, heterogeneous nucleation was significantly promoted, leading to grain refinement.
 - v. For AM solidification, the addition of appropriate solutes to generate sufficient ΔT and thereby to counteract the effect of the thermal gradient is the prerequisite for the activation of heterogenous nucleation.

Author Contributions: Conceptualization, Q.T. and M.-X.Z.; methodology, Q.T. and Y.Y.; validation, Q.T. and M.-X.Z.; formal analysis, Q.T.; investigation, Q.T. and Y.Y.; data curation, Q.T.; writing—original draft preparation, Q.T.; writing—review and editing, Q.T. and M.-X.Z.; visualization, Q.T.; supervision, M.-X.Z.; project administration, M.-X.Z.; funding acquisition, M.-X.Z. All authors have read and agreed to the published version of the manuscript.

Funding: This research was funded by Australia Research Council (ARC) grant number [DP210103162].

Data Availability Statement: The raw and processed data required to reproduce these findings are available by contacting the corresponding author.

Acknowledgments: The authors thank the Australian Microscopy & Microanalysis Research Facility at the Centre for Microscopy and Microanalysis (CMM), The University of Queensland for the facilities and technical assistance.

Conflicts of Interest: The authors declare no conflict of interest.

References

1. DebRoy, T.; Wei, H.L.; Zuback, J.S.; Mukherjee, T.; Elmer, J.W.; Milewski, J.O.; Beese, A.M.; Wilson-Heid, A.; De, A.; Zhang, W. Additive manufacturing of metallic components—Process, structure and properties. *Prog. Mater. Sci.* **2018**, *92*, 112–224. [[CrossRef](#)]
2. Bermingham, M.; StJohn, D.; Easton, M.; Yuan, L.; Dargusch, M. Revealing the Mechanisms of Grain Nucleation and Formation During Additive Manufacturing. *JOM* **2020**, *72*, 1065–1073. [[CrossRef](#)]
3. Zhang, D.; Prasad, A.; Bermingham, M.J.; Todaro, C.J.; Benoit, M.J.; Patel, M.N.; Qiu, D.; StJohn, D.H.; Qian, M.; Easton, M.A. Grain Refinement of Alloys in Fusion-Based Additive Manufacturing Processes. *Metall. Mater. Trans. A* **2020**, *51*, 4341–4359. [[CrossRef](#)]
4. Tan, Q.; Liu, Y.; Fan, Z.; Zhang, J.; Yin, Y.; Zhang, M.X. Effect of processing parameters on the densification of an additively manufactured 2024 Al alloy. *J. Mater. Sci. Technol.* **2020**, *58*, 34–45. [[CrossRef](#)]
5. Bermingham, M.J.; StJohn, D.H.; Krynen, J.; Tedman-Jones, S.; Dargusch, M.S. Promoting the columnar to equiaxed transition and grain refinement of titanium alloys during additive manufacturing. *Acta Mater.* **2019**, *168*, 261–274. [[CrossRef](#)]
6. Wang, Z.; Palmer, T.A.; Beese, A.M. Effect of processing parameters on microstructure and tensile properties of austenitic stainless steel 304L made by directed energy deposition additive manufacturing. *Acta Mater.* **2016**, *110*, 226–235. [[CrossRef](#)]
7. Thijs, L.; Kempen, K.; Kruth, J.-P.; Van Humbeeck, J. Fine-structured aluminium products with controllable texture by selective laser melting of pre-alloyed AlSi10Mg powder. *Acta Mater.* **2013**, *61*, 1809–1819. [[CrossRef](#)]
8. Aboulkhair, N.T.; Simonelli, M.; Parry, L.; Ashcroft, I.; Tuck, C.; Hague, R. 3D printing of Aluminium alloys: Additive Manufacturing of Aluminium alloys using selective laser melting. *Prog. Mater. Sci.* **2019**, *106*, 100578. [[CrossRef](#)]
9. Gourlay, C.M.; Dahle, A.K. Dilatant shear bands in solidifying metals. *Nature* **2007**, *445*, 70. [[CrossRef](#)]
10. Nafisi, S.; Ghomashchi, R. *Semi-Solid Processing of Aluminum Alloys*; Springer International Publishing: Cham, Switzerland, 2016.
11. Easton, M.; StJohn, D. Grain refinement of aluminum alloys: Part I. the nucleant and solute paradigms—A review of the literature. *Metall. Mater. Trans. A* **1999**, *30*, 1613–1623. [[CrossRef](#)]

12. Easton, M.; StJohn, D. Grain refinement of aluminum alloys: Part II. Confirmation of, and a mechanism for, the solute paradigm. *Metall. Mater. Trans. A* **1999**, *30*, 1625–1633. [[CrossRef](#)]
13. Martin, J.H.; Yahata, B.D.; Hundley, J.M.; Mayer, J.A.; Schaedler, T.A.; Pollock, T.M. 3D printing of high-strength aluminium alloys. *Nature* **2017**, *549*, 365. [[CrossRef](#)] [[PubMed](#)]
14. Li, X.P.; Ji, G.; Chen, Z.; Addad, A.; Wu, Y.; Wang, H.W.; Vleugels, J.; Van Humbeeck, J.; Kruth, J.P. Selective laser melting of nano-TiB₂ decorated AlSi10Mg alloy with high fracture strength and ductility. *Acta Mater.* **2017**, *129*, 183–193. [[CrossRef](#)]
15. Tan, Q.; Zhang, J.; Mo, N.; Fan, Z.; Yin, Y.; Bermingham, M.; Liu, Y.; Huang, H.; Zhang, M.-X. A novel method to 3D-print fine-grained AlSi10Mg alloy with isotropic properties via inoculation with LaB₆ nanoparticles. *Addit. Manuf.* **2020**, *32*, 101034. [[CrossRef](#)]
16. Tan, Q.; Zhang, J.; Sun, Q.; Fan, Z.; Li, G.; Yin, Y.; Liu, Y.; Zhang, M.-X. Inoculation treatment of an additively manufactured 2024 aluminium alloy with titanium nanoparticles. *Acta Mater.* **2020**, *196*, 1–16. [[CrossRef](#)]
17. Jia, Q.; Rometsch, P.; Kürsteiner, P.; Chao, Q.; Huang, A.; Weyland, M.; Bourgeois, L.; Wu, X. Selective laser melting of a high strength AlMnSc alloy: Alloy design and strengthening mechanisms. *Acta Mater.* **2019**, *171*, 108–118. [[CrossRef](#)]
18. Mair, P.; Goettgens, V.S.; Rainer, T.; Weinberger, N.; Letofsky-Papst, I.; Mitsche, S.; Leichtfried, G. Laser powder bed fusion of nano-CaB₆ decorated 2024 aluminum alloy. *J. Alloys Compd.* **2021**, *863*, 158714. [[CrossRef](#)]
19. Mair, P.; Kaserer, L.; Braun, J.; Stajkovic, J.; Klein, C.; Schimbäck, D.; Perfler, L.; Zhuravlev, E.; Kessler, O.; Leichtfried, G. Dependence of mechanical properties and microstructure on solidification onset temperature for Al2024–CaB₆ alloys processed using laser powder bed fusion. *Mater. Sci. Eng. A* **2022**, *833*, 142552. [[CrossRef](#)]
20. Xi, L.; Xu, J.; Gu, D.; Feng, L.; Lu, Q.; Prashanth, K.G. A novel crack-free and refined 2195-Ti/CeB₆ composites prepared by laser powder bed fusion. *Mater. Lett.* **2023**, *333*, 133572. [[CrossRef](#)]
21. Martin, J.H.; Yahata, B.; Mayer, J.; Mone, R.; Stonkevitch, E.; Miller, J.; O'Masta, M.R.; Schaedler, T.; Hundley, J.; Callahan, P.; et al. Grain refinement mechanisms in additively manufactured nano-functionalized aluminum. *Acta Mater.* **2020**, *200*, 1022–1037. [[CrossRef](#)]
22. Rometsch, P.A.; Zhu, Y.; Wu, X.; Huang, A. Review of high-strength aluminium alloys for additive manufacturing by laser powder bed fusion. *Mater. Des.* **2022**, *219*, 110779. [[CrossRef](#)]
23. Schmidtke, K.; Palm, F.; Hawkins, A.; Emmelmann, C. Process and Mechanical Properties: Applicability of a Scandium modified Al-alloy for Laser Additive Manufacturing. *Phy. Procedia* **2011**, *12*, 369–374. [[CrossRef](#)]
24. Spierings, A.B.; Dawson, K.; Heeling, T.; Uggowitz, P.J.; Schäublin, R.; Palm, F.; Wegener, K. Microstructural features of Sc- and Zr-modified Al-Mg alloys processed by selective laser melting. *Mater. Des.* **2017**, *115*, 52–63. [[CrossRef](#)]
25. Zhu, Z.; Ng, F.L.; Seet, H.L.; Lu, W.; Liebscher, C.H.; Rao, Z.; Raabe, D.; Mui Ling Nai, S. Superior mechanical properties of a selective-laser-melted AlZnMgCuScZr alloy enabled by a tunable hierarchical microstructure and dual-nanoprecipitation. *Mater. Today* **2022**, *52*, 90–101. [[CrossRef](#)]
26. Liu, X.; Liu, Y.; Zhou, Z.; Zhan, Q. Enhanced strength and ductility in Al-Zn-Mg-Cu alloys fabricated by laser powder bed fusion using a synergistic grain-refining strategy. *J. Mater. Sci. Technol.* **2022**, *124*, 41–52. [[CrossRef](#)]
27. Turnbull, D.; Vonnegut, B. Nucleation Catalysis. *Ind. Eng. Chem.* **1952**, *44*, 1292–1298. [[CrossRef](#)]
28. Mohanty, P.S.; Gruzleski, J.E. Mechanism of grain refinement in aluminium. *Acta Metall. Mater.* **1995**, *43*, 2001–2012. [[CrossRef](#)]
29. Michael Rajan, H.B.; Ramabalan, S.; Dinaharan, I.; Vijay, S.J. Synthesis and characterization of in situ formed titanium diboride particulate reinforced AA7075 aluminum alloy cast composites. *Mater. Des.* **2013**, *44*, 438–445. [[CrossRef](#)]
30. Wang, F.; Liu, Z.; Qiu, D.; Taylor, J.A.; Easton, M.A.; Zhang, M.-X. Revisiting the role of peritectics in grain refinement of Al alloys. *Acta Mater.* **2013**, *61*, 360–370. [[CrossRef](#)]
31. Li, Q.; Li, G.; Lin, X.; Zhu, D.; Jiang, J.; Shi, S.; Liu, F.; Huang, W.; Vanmeensel, K. Development of a high strength Zr/Sc/Hf-modified Al-Mn-Mg alloy using Laser Powder Bed Fusion: Design of a heterogeneous microstructure incorporating synergistic multiple strengthening mechanisms. *Addit. Manuf.* **2022**, *57*, 102967. [[CrossRef](#)]
32. Easton, M.; StJohn, D. An analysis of the relationship between grain size, solute content, and the potency and number density of nucleant particles. *Metall. Mater. Trans. A* **2005**, *36*, 1911–1920. [[CrossRef](#)]
33. Tan, Q.; Yin, Y.; Fan, Z.; Zhang, J.; Liu, Y.; Zhang, M.-X. Uncovering the roles of LaB₆-nanoparticle inoculant in the AlSi10Mg alloy fabricated via selective laser melting. *Mater. Sci. Eng. A* **2021**, *800*, 140365. [[CrossRef](#)]
34. Tan, Q.; Fan, Z.; Tang, X.; Yin, Y.; Li, G.; Huang, D.; Zhang, J.; Liu, Y.; Wang, F.; Wu, T.; et al. A novel strategy to additively manufacture 7075 aluminium alloy with selective laser melting. *Mater. Sci. Eng. A* **2021**, *821*, 141638. [[CrossRef](#)]
35. Qi, T.; Zhu, H.; Zhang, H.; Yin, J.; Ke, L.; Zeng, X. Selective laser melting of Al7050 powder: Melting mode transition and comparison of the characteristics between the keyhole and conduction mode. *Mater. Des.* **2017**, *135*, 257–266. [[CrossRef](#)]
36. Tan, Q.; Chang, H.; Yin, Y.; Wang, F.; Huang, D.; Liang, G.; Wu, T.; Yan, M.; Cheng, X.; Zhang, M.-X. Simultaneous enhancements of strength and ductility of a selective laser melted H13 steel through inoculation treatment. *Scr. Mater.* **2022**, *219*, 114874. [[CrossRef](#)]
37. Liu, X.; Liu, Y.; Zhou, Z.; Zhong, H.; Zhan, Q. A combination strategy for additive manufacturing of AA2024 high-strength aluminium alloys fabricated by laser powder bed fusion: Role of hot isostatic pressing. *Mater. Sci. Eng. A* **2022**, *850*, 143597. [[CrossRef](#)]
38. Zhang, H.; Zhu, H.; Qi, T.; Hu, Z.; Zeng, X. Selective laser melting of high strength Al–Cu–Mg alloys: Processing, microstructure and mechanical properties. *Mater. Sci. Eng. A* **2016**, *656*, 47–54. [[CrossRef](#)]

39. Hu, Z.; Nie, X.; Qi, Y.; Zhang, H.; Zhu, H. Cracking criterion for high strength Al–Cu alloys fabricated by selective laser melting. *Addit. Manuf.* **2021**, *37*, 101709. [[CrossRef](#)]
40. Zhang, J.; Gao, J.; Song, B.; Zhang, L.; Han, C.; Cai, C.; Zhou, K.; Shi, Y. A novel crack-free Ti-modified Al-Cu-Mg alloy designed for selective laser melting. *Addit. Manuf.* **2021**, *38*, 101829. [[CrossRef](#)]
41. Zhu, X.; Zhu, Z.; Liu, T.; Liao, W.; Du, Y.; Wei, H. Crack-free and high-strength AA2024 alloy obtained by additive manufacturing with controlled columnar-equiaxed-transition. *J. Mater. Sci. Technol.* **2023**, *156*, 183–196. [[CrossRef](#)]
42. Liu, X.; Liu, Y.; Zhou, Z.; Wang, K.; Zhan, Q.; Xiao, X. Grain refinement and crack inhibition of selective laser melted AA2024 aluminum alloy via inoculation with TiC–TiH₂. *Mater. Sci. Eng. A* **2021**, *813*, 141171. [[CrossRef](#)]
43. Roscher, M.; Balachandran, S.; Mayweg, D.; Jäggle, E. Development of Al-Ti-based alloys for laser powder bed fusion. *Addit. Manuf.* **2021**, *47*, 102315. [[CrossRef](#)]
44. Winegard, W.; Chalmers, B. Supercooling and dendritic freezing in alloys. *Trans. Am. Soc. Met.* **1954**, *46*, 1214–1224.
45. StJohn, D.H.; Qian, M.; Easton, M.A.; Cao, P. The Interdependence Theory: The relationship between grain formation and nucleant selection. *Acta Mater.* **2011**, *59*, 4907–4921. [[CrossRef](#)]
46. Xu, Y.; Casari, D.; Mathiesen, R.H.; Li, Y. Revealing the heterogeneous nucleation behavior of equiaxed grains of inoculated Al alloys during directional solidification. *Acta Mater.* **2018**, *149*, 312–325. [[CrossRef](#)]
47. Wang, L.; Yang, L.; Zhang, D.; Xia, M.; Wang, Y.; Li, J.G. The Role of Lattice Misfit on Heterogeneous Nucleation of Pure Aluminum. *Metall. Mater. Trans. A* **2016**, *47*, 5012–5022. [[CrossRef](#)]
48. Wang, L.; Lu, W.; Hu, Q.; Xia, M.; Wang, Y.; Li, J.-g. Interfacial tuning for the nucleation of liquid AlCu alloy. *Acta Mater.* **2017**, *139*, 75–85. [[CrossRef](#)]
49. Fan, Z.; Men, H.; Wang, Y.; Que, Z. A New Atomistic Mechanism for Heterogeneous Nucleation in the Systems with Negative Lattice Misfit: Creating a 2D Template for Crystal Growth. *Metals* **2021**, *11*, 478. [[CrossRef](#)]
50. Fan, Z.; Men, H.J.M.R.E. A molecular dynamics study of heterogeneous nucleation in generic liquid/substrate systems with positive lattice misfit. *Mater. Res. Express* **2020**, *7*, 126501. [[CrossRef](#)]
51. Shu, D.; Sun, B.; Mi, J.; Grant, P.S. A quantitative study of solute diffusion field effects on heterogeneous nucleation and the grain size of alloys. *Acta Mater.* **2011**, *59*, 2135–2144. [[CrossRef](#)]
52. Kurz, W.; Fisher, D.J. *Fundamentals of Solidification*; ASM International: Almere, The Netherlands, 1992.
53. Tan, Q.; Yin, Y.; Prasad, A.; Li, G.; Zhu, Q.; StJohn, D.H.; Zhang, M.-X. Demonstrating the roles of solute and nucleant in grain refinement of additively manufactured aluminium alloys. *Addit. Manuf.* **2022**, *49*, 102516. [[CrossRef](#)]
54. Patel, M.N.; Qiu, D.; Wang, G.; Gibson, M.A.; Prasad, A.; StJohn, D.H.; Easton, M.A. Understanding the refinement of grains in laser surface remelted Al–Cu alloys. *Scr. Mater.* **2020**, *178*, 447–451. [[CrossRef](#)]
55. Prasad, A.; Yuan, L.; Lee, P.; Patel, M.; Qiu, D.; Easton, M.; StJohn, D. Towards understanding grain nucleation under Additive Manufacturing solidification conditions. *Acta Mater.* **2020**, *195*, 392–403. [[CrossRef](#)]
56. Soysal, T.; Kou, S. A simple test for assessing solidification cracking susceptibility and checking validity of susceptibility prediction. *Acta Mater.* **2018**, *143*, 181–197. [[CrossRef](#)]
57. Li, G.; Huang, Y.; Li, X.; Guo, C.; Zhu, Q.; Lu, J. Laser powder bed fusion of nano-titania modified 2219 aluminium alloy with superior mechanical properties at both room and elevated temperatures: The significant impact of solute. *Addit. Manuf.* **2022**, *60*, 103296. [[CrossRef](#)]
58. Li, H.-y.; Li, D.-w.; Zhu, Z.-x.; Chen, B.-a.; Chen, X.; Yang, C.-l.; Zhang, H.-y.; Kang, W. Grain refinement mechanism of as-cast aluminum by hafnium. *Trans. Nonferrous Met. Soc. China* **2016**, *26*, 3059–3069. [[CrossRef](#)]
59. Wang, Z.; Wang, X.; Chen, X.; Qiu, C. Complete columnar-to-equiaxed transition and significant grain refinement in an aluminium alloy by adding Nb particles through laser powder bed fusion. *Addit. Manuf.* **2022**, *51*, 102615. [[CrossRef](#)]
60. Xiao, F.; Wang, S.; Wang, Y.; Shu, D.; Zhu, G.; Sun, B.; StJohn, D. Niobium nanoparticle-enabled grain refinement of a crack-free high strength Al-Zn-Mg-Cu alloy manufactured by selective laser melting. *J. Alloys Compd.* **2022**, *900*, 163427. [[CrossRef](#)]
61. Li, X.; Li, D.; Li, G.; Cai, Q. Microstructure, mechanical properties, aging behavior, and corrosion resistance of a laser powder bed fusion fabricated Al–Zn–Mg–Cu–Ta alloy. *Mater. Sci. Eng. A* **2022**, *832*, 142364. [[CrossRef](#)]

Disclaimer/Publisher’s Note: The statements, opinions and data contained in all publications are solely those of the individual author(s) and contributor(s) and not of MDPI and/or the editor(s). MDPI and/or the editor(s) disclaim responsibility for any injury to people or property resulting from any ideas, methods, instructions or products referred to in the content.